Detection of Electron Paramagnetic Resonance of Two Electron Spins Using a Single NV Center in Diamond

Yuhang Ren^{1, a)} and Susumu Takahashi^{1, 2, b)}

¹⁾Department of Physics and Astronomy, University of Southern California, Los Angeles, 90089. CA, USA

²⁾Department of Chemistry, University of Southern California, Los Angeles, 90089. CA, USA

(Dated: 30 July 2024)

An interacting spin system is a great testbed for fundamental quantum physics and applications in quantum sensing and quantum simulation. For these investigations, detailed information of the interactions, e.g. the number of spins and their interaction strengths, is often required. In this study, we present the identification and characterization of a single nitrogen-vacancy (NV) center coupled to two electron spins. In the experiment, we first identify a well isolated single NV center, and characterize its spin decoherence time. Then we perform NV-detected electron paramagnetic resonance (EPR) spectroscopy to detect surrounding electron spins. From the analysis of the NV-EPR signal, we determine the number of detected spins and their interaction strengths precisely. Moreover, the spectral analysis indicates candidates of the detected spins to be diamond surface spins. This study demonstrates a promising approach for the identification and characterization of an interacting spin system for realizing entangled sensing, using the electron spin as quantum reporters.

Keywords: EPR, Quantum Sensing, NV Center

a)Electronic mail: yuhangre@usc.edu

b)Electronic mail: susumuta@usc.edu

I. INTRODUCTION

A nitrogen-vacancy (NV) center is a fluorescent impurity center existing in the diamond lattice¹. The unique electronic structure of the NV center allows the polarization and readout of the the spin state through optical excitation and optically detected magnetic resonance (ODMR) technique^{2–4}. The NV center also has a long spin coherence time at room temperature^{5–7}. It has been shown to be a promising quantum sensor, enabling measurement of an extremely small magnetic field^{8–11}, magnetic resonance spectroscopy with single spin sensitivity^{12–19}, and quantum simulations^{20–22}.

A system with interacting spins is a great platform for fundamental physics and applications in quantum information science. For example, a network of NV spins can be a great candidate to build an entangled quantum sensor with enhanced sensitivity²³. Interacting spin systems also exhibit novel phases and dynamics such as spin liquids, time crystals and non-equilibrium dynamics^{24–27}. NV-detected electron paramagnetic resonance (NV-EPR) spectroscopy with a single NV center is a powerful method to study nanoscale environments of interacting spins. NV-EPR can determine the number and type of spins surrounding the NV center. It can also determine the coupling strengths between the NV and each surrounding electron spin^{14,18}. NV-EPR has been demonstrated to detect P1 centers, N2 centers and other unidentified spins^{18,28–32}. Moreover, naturally occurring electron spins on diamond surfaces have been demonstrated to be quantum reporters for improved sensing capabilities³³. A characterizable and controllable network of quantum reporter spins can be potentially used for entanglement-enhanced surface quantum sensing. However, only few demonstrations have been performed to determine the number of interacting electron spins and individual coupling strength to NV center^{13,33}. This remains a challenge for single NV-EPR detection.

In this work, we discuss the demonstration of NV-EPR spectroscopy of a few electron spins. We employ a single shallow NV center in diamond as a sensor and utilize a double electron-electron resonance (DEER) technique to show the detection of EPR signals of surrounding spins. The observation of the NV-EPR signal confirms the detection of spins. The type of the detected spin is analyzed from their g-values and hyperfine splitting. Moreover, we present a simple model to determine the number of the detected spins and the strengths of their magnetic dipole interactions. We find a single NV center coupled to two electron spins with dipolar coupling 1.12 ± 0.13 MHz and 2.24 ± 0.17 MHz from the analysis of the NV-EPR signal. The presented spin system

will be useful for the investigation of quantum effects that requires a low number of spins³⁴ or open quantum dynamics³⁵. The experimental methods can be used to realize entangled quantum reporters for quantum sensing.

II. EXPERIMENTAL SETUP

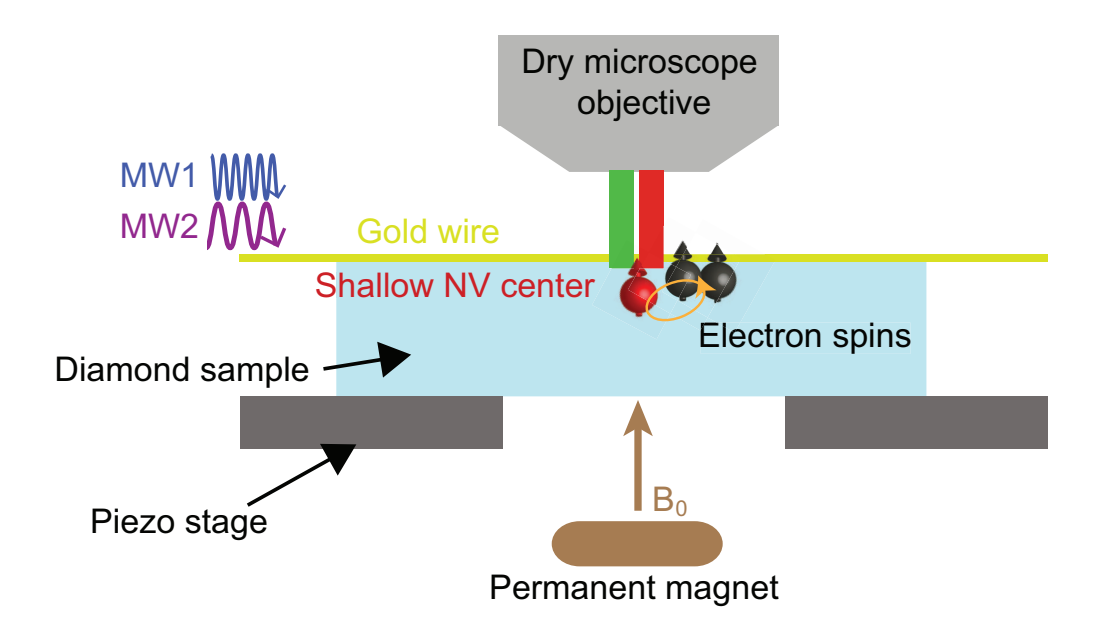


FIG. 1. Illustration of the experimental setup. A (111)-cut diamond sample is mounted on a piezo stage. A disk magnet is used to provides static external field B_0 and a gold wire is attached on the sample to provide microwave excitation, MW1 and MW2. A 532 nm laser is focused onto a shallow NV near the surface of the diamond with a dry microscope objective. PL is collected through the same objective and detected with a photon detector.

In this study, we employ single NV centers in a diamond crystal sample purchased from Qnami³⁶. The sample is a (111)-cut, specially designed diamond. Shallow NVs (\sim 10 nm depth) were created with Nitrogen ion implantation with the energy of 6 keV and subsequent annealing process. The sample has a unique nano-pillar structure that allows easy isolation and identification of single NV centers. We have studied multiple single NV centers in this sample. In the present paper, our investigation focuses on one of the single NV centers with an unique NV-EPR signal.

The setup of the experiment is illustrated in Fig. 1. The diamond sample is mounted on a XYZ piezo stage. A permanent disk magnet is placed under the stage to provide a static magnetic field (B_0) along the [111] direction of the diamond lattice. For ODMR spectroscopy of the NV cen-

ter, two channels of microwave (MW1 and MW2) excitation are applied using sources (Stanford SG386) and an amplifier (Mini-Circuits ZHL-15W-422-S+). Both MW1 and MW2 excitation is applied with a 20um diameter gold wire attached close to the top of the sample. A diode-pumped solid-state laser (CrystaLaser, 100 mW) and a microscope dry objective (ZEISS, 100x, NA = 0.8) are employed for the laser excitation. Photoluminescence (PL) from the NV center is collected by the same objective and redirected by a dichroic mirror towards an avalanche photon detector (Excelitas, SPCM-AQRH-13-FC). A central computer is used to control the microwave and laser pulses and analyze the photon counts signal.

III. RESULTS AND DISCUSSION

The NV-EPR experiment starts with the characterization of external magnetic field and the coherent manipulation capability of the NV centers. After identifying single NV centers using the auto-correlation experiment and ODMR spectroscopy¹⁴, we focus on our investigation into each single NV (See Fig. 2(a)), and perform a pulsed ODMR measurement to determine the magnetic field strength and tilt angle. As shown in Fig. 2(b), the laser pulse with a duration of 5 μ s initialize (Init) the NV state to $|m_S = 0\rangle$. After a short delay (\sim 1 μ s), a MW1 (π) $_Y$ pulse is applied to drive a rotation of the spin in the Bloch's sphere along the x-axis (see Fig. 2(b)), from brighter $|m_S = 0\rangle$ to darker $|m_S = \pm 1\rangle$ spin states. Afterwards a short readout (RO) laser pulse with a duration of 300 ns project NV's coherent spin state into the population difference, which is measured by the PL intensity, resulting in observation of ODMR signals at the $|m_S = 0\rangle \leftrightarrow |m_S = +1\rangle$ and $|m_S = 0\rangle \leftrightarrow |m_S = -1\rangle$ transition frequencies. Fig. 2(d) shows the PL intensity as a function of the MW1 frequency. By fitting the two frequencies to the following NV Hamiltonian, we obtain the magnetic field strength (B_0) and the tilt angle (θ) of the magnetic field in respect to the NV axis,

$$H = \gamma_{NV} B_0 \left(\sin\theta \cdot S_x + \cos\theta \cdot S_z \right) + DS_z^2, \tag{1}$$

where γ_{NV} is the gyromagnetic ratio of the NV spin (28.024 GHz/Tesla). $S=(S_x,S_y,S_z)$ are the spin operators of S=1. D is the NV zero-field energy splitting (2.87 GHz). The fit gives the magnetic field strength of $B_0=32.59\pm0.02$ mT and the tilt angle of $\theta=3.5\pm0.8$ degrees. Next we perform a measurement of Rabi oscillations. The pulse sequences of the experiment is shown in Fig. 2(c). After the laser pulse initialization, a MW1 $(\pi)_Y$ pulse at the NV Larmor frequency of 3783.39 MHz (corresponding to the transition $|m_S=0\rangle \leftrightarrow |m_S=+1\rangle$) with a duration of T_{SWP}

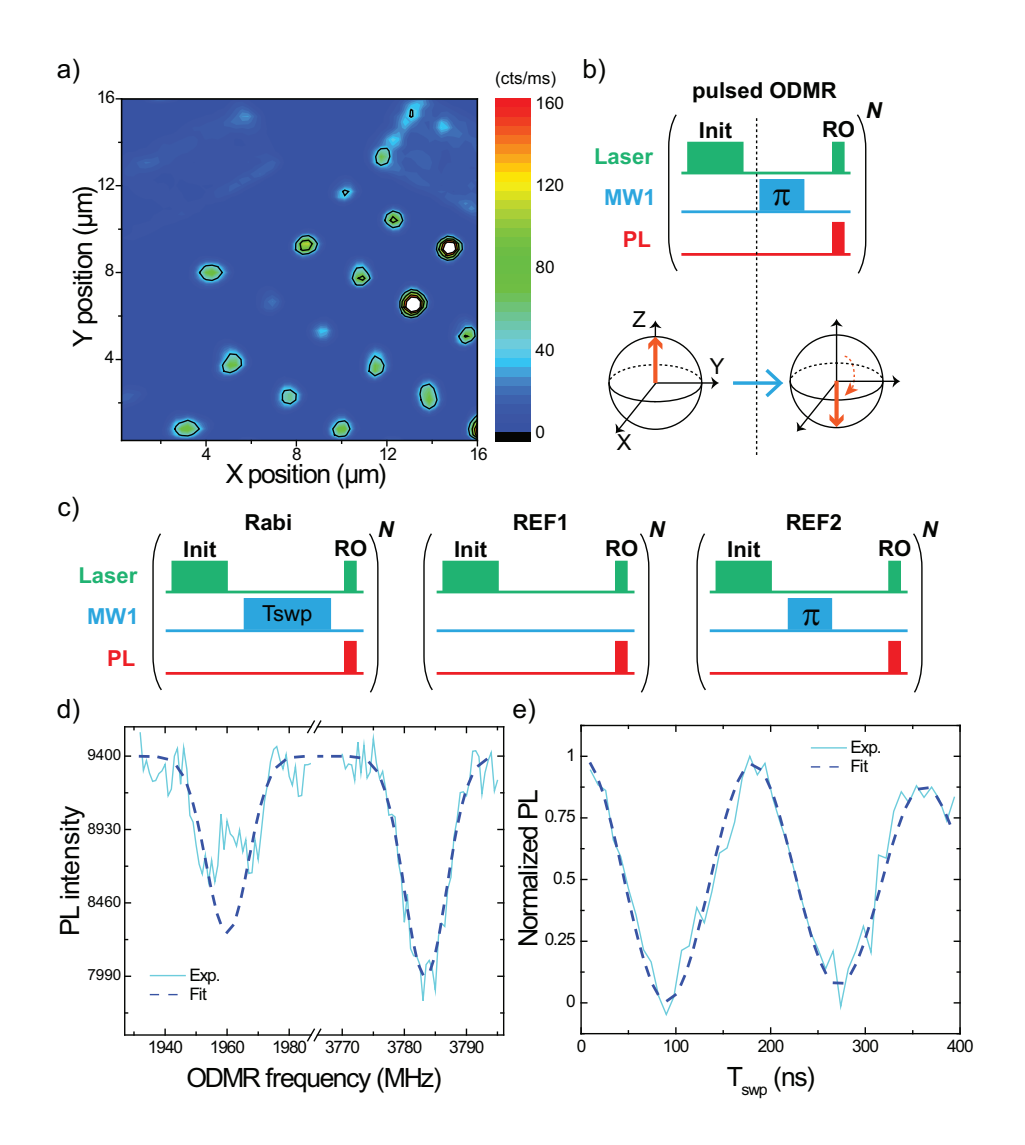


FIG. 2. Characterization of a single NV center. (a) PL image of the diamond sample. The PL signals are from single NV centers. (b) Pulse sequence for pulsed ODMR measurement. The spin starts at $|m_S=0\rangle$ after initialization laser pulse (indicated as Init), and evolve under the effect of the MW1 pulse. The readout laser pulse (indicated as RO) measures PL level according to the projected population difference. N = 100,000 is the number of pulse sequences used for averaging. (c) Pulse sequences for Rabi Oscillation measurement. Two reference channels (REF1 and REF2) are used for PL normalization. N = 100,000. (d) Pulsed ODMR data. By fitting with Gaussian peak functions, the peak frequencies are extracted to obtain magnetic field and tilt angle from fitting with the NV Hamiltonian. (e) Rabi oscillation data. MW1 frequency is set to $|m_S=0\rangle \leftrightarrow |m_S=+1\rangle$ transition frequency at 3783.39 MHz while the length of MW1 pulse T_{swp} is swept. PL is normalized by $\frac{Rabi-REF2}{REF1-REF2}$. Rabi oscillation frequency f of 5.50 ± 0.03 MHz and decay time T_0 of 0.67 ± 0.08 μs is obtained from a fit to $\frac{1}{2}\cdot(1+exp(-(t/T_0)^2)cos(2\pi ft))$.

is applied. Then, the resultant population change is readout with the RO laser pulse. Two additional reference channels (REF1 and REF2) are used for data normalization. REF1 corresponds to maximum PL detected in Rabi measurement and REF2 corresponds to minimum PL. The normalized PL is (Rabi-REF2)/(REF1-REF2). This normalization procedure will reduce degrees of freedom in data fitting. As shown in Fig. 2(e), the normalized PL shows oscillations as the MW1 pulse length is varied. This is the Rabi oscillations proving the coherent manipulation of the NV spin states. From the period of the oscillations, the duration of the pulses can be determined. In the present case, we used a cosine oscillation containing a Gaussian decay¹⁴, and obtained the π , $\pi/2$ and $3\pi/2$ pulse duration to be 46, 92 and 138 ns, respectively.

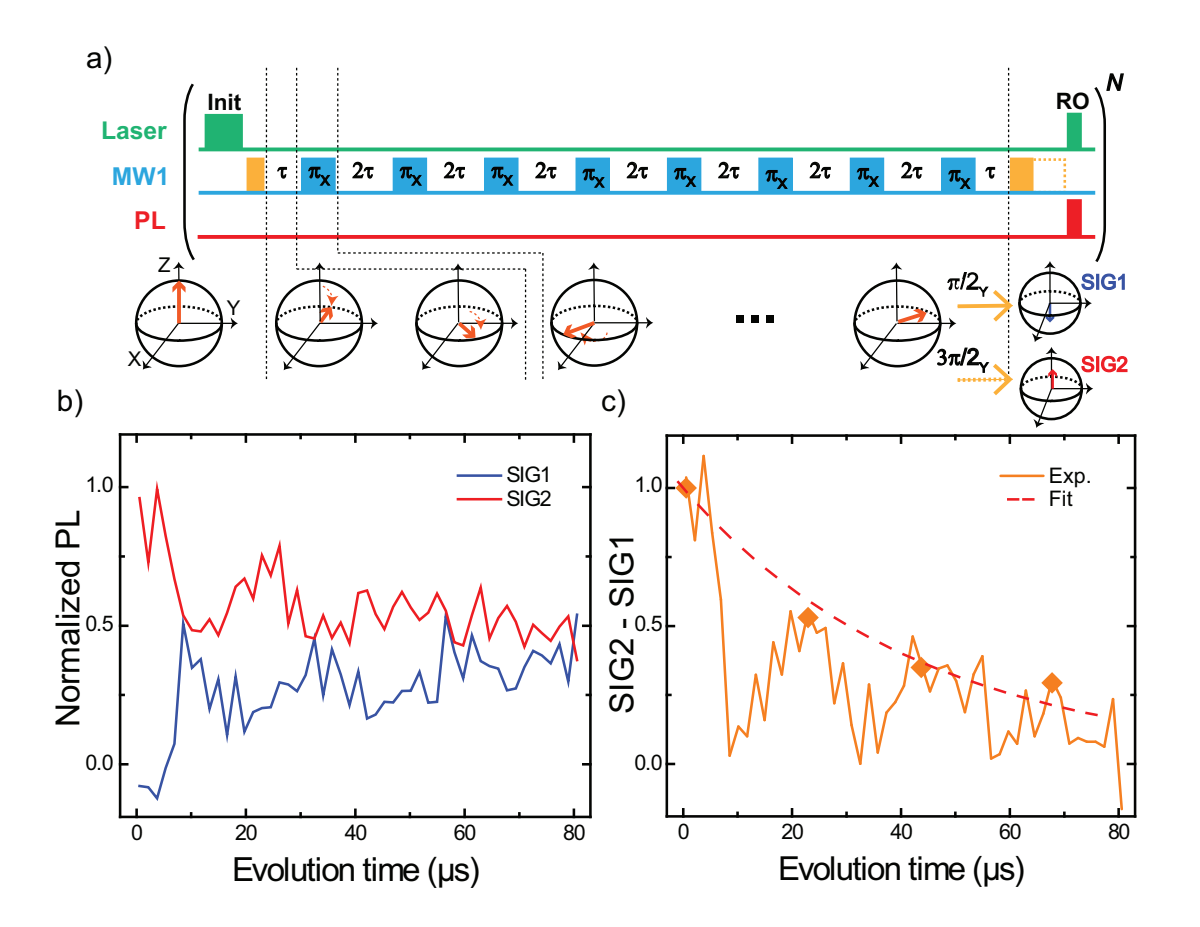


FIG. 3. CPMG-8 sequence and data. (a) CPMG-8 sequence. The yellow and blue MW1 pulses are with X/Y phases. SIG1 channel uses a $(\pi/2)_Y$ pulse to project the phase into population difference, while SIG2 channel uses a $(3\pi/2)_Y$ pulse (indicated with dashed yellow box). N = 220,000. (b) CPMG-8 data showing normalized PL. (c) The envelop of the normalized signal (SIG2 - SIG1), indicated by the orange envelop peak points, is fit to a exponential decay and we extract a T_2 time of $44 \pm 5 \,\mu$ s. Additional modulation on the signal is observed due to ESEEM effect.

Next, we characterize the spin decoherence time (T_2) using a Carr-Purcell-Meiboom-Gill sequence. The particular sequence used contains eight π pulses which is referred to later as a CPMG-8 sequence (see Fig. 3(a)). In the CPMG-8 experiment, after the preparation of the superposition state $\frac{1}{\sqrt{2}}(|+1\rangle+|0\rangle)$ by the $(\pi/2)_Y$ pulse, a chain of $(\pi)_X$ pulses are applied at every 2τ to keep the coherence state for an extended period. The resultant coherent state is mapped into the $|m_s=0\rangle$ state with the application of the second $(\pi/2)_Y$ pulse (SIG1). In addition, in a different signal channel, we use a $(3\pi/2)_Y$ pulse instead of the $(\pi/2)_Y$ pulse to map the state into the $|m_s=1\rangle$ state (SIG2). Two signal channels are used to improve the signal-to-noise ratio (SNR) by removing systematic noise and doubling signal contrast. PL intensity is normalized using the same method used in the Rabi oscillation experiment. As seen in Fig. 3(b), a oscillating and decaying difference in the normalized PL is observed. We analyze the data by fitting the difference (SIG2-SIG1) with a exponential decay and obtain the relaxation time constant T_2 (See Fig. 3(c)). The data also shows the electron spin echo envelope modulation (ESEEM) at a modulation frequency of 11.7 MHz, indicating couplings to nuclear spins in proximity.

Finally, we perform NV-detected EPR (NV-EPR) spectroscopy to detect electron spins surrounding the NV center. In the NV-EPR experiment, we use a DEER sequence shown in Fig. 4(a). We use two microwaves (MW1 and MW2) to coherently control the NV spin and target environment spins, respectively. The first microwave (MW1) is fixed at NV Lamour frequency. The second microwave (MW2) is swept in frequency, and when the frequency of MW2 is at the Lamour frequency of the target spins, the MW2 pulse flips the target spins. As can be seen from Fig. 4(a), the sequence consists of the CPMG component for the NV spin and the π pulses for the target spins (denoted as CPMG-DEER). In the CPMG-DEER experiment, first, the NV's spin state is prepared into $|\psi_0\rangle = \frac{1}{\sqrt{2}}(|+1\rangle + |0\rangle)$ state. The spin state is sensitive to small change in external magnetic field B_0 , which in our case is total dipole field B_{dip} from surrounding electron spins. In the present case, with the application of the π pulses with MW2 (See Fig. 4(a)), phase shifts due to changes of the magnetic field is accumulated to the NV coherent state, i.e. $|\psi_0\rangle \rightarrow |\psi\rangle = \frac{1}{\sqrt{2}}(|+1\rangle + e^{i\delta\phi}|0\rangle$). The phase shifts can be modeled as,

$$\delta\phi = \frac{\gamma_{NV}}{\hbar} \left[\int_0^{\tau} B_{dip}(t)dt - \int_{\tau}^{3\tau} B_{dip}(t)dt + \dots + \int_{13\tau}^{15\tau} B_{dip}(t)dt - \int_{15\tau}^{16\tau} B_{dip}(t)dt \right], \quad (2)$$

where \hbar is the reduced Planck constant. The pulse length is relatively short compare to τ time so the evolution during pulses are neglected in the equation. The spin flip-flop not due to pulse

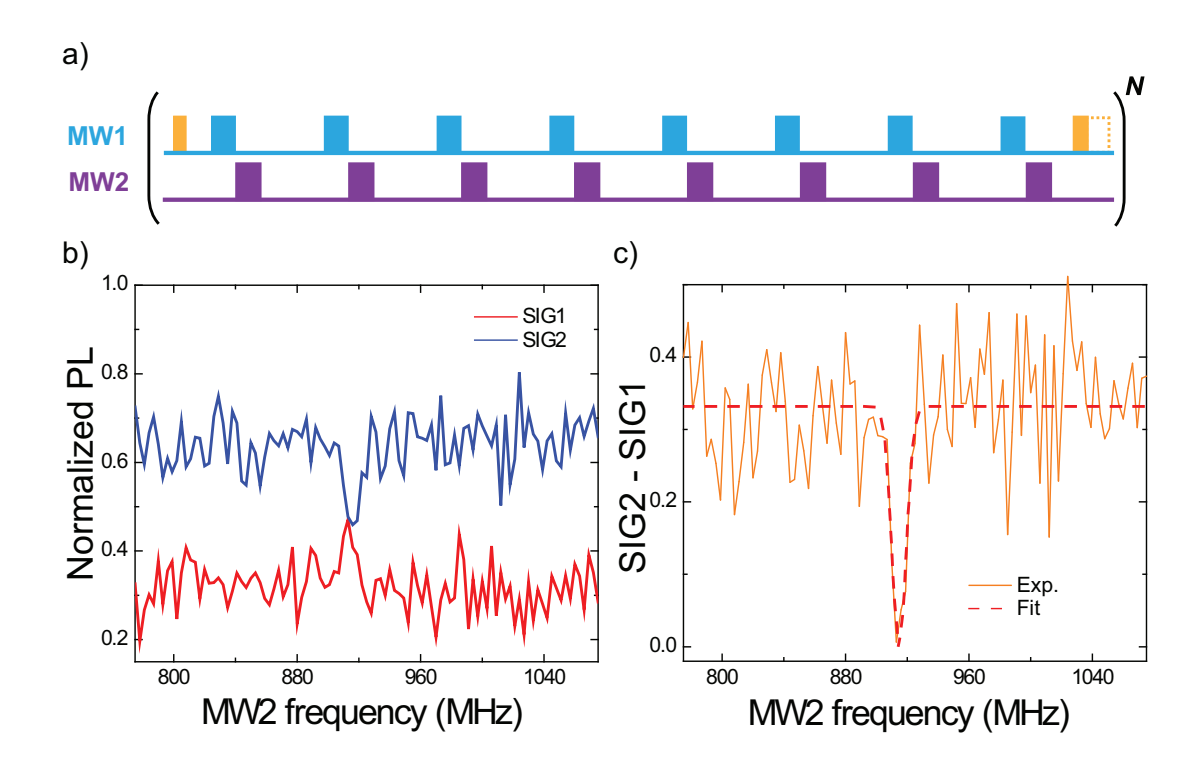


FIG. 4. NV-EPR sequence and data. (a) Highlight of the CPMG-DEER sequence showing only the MW1 and MW2 pulses, indicated by blue and purple boxes, respectively. τ time is set to 1.28 μ s and the total sensing time is 20.864 μ s. N = 1,325,000. (b) CPMG-DEER data. Both SIG1 and SIG2 channels are used. The signals are normalized in the same way as CPMG experiment. (c) By fitting the difference (SIG2-SIG1) to a Gaussian peak function, we obtain the narrow DEER spectrum centered at 914.7 \pm 0.9 MHz, with no sign of hyperfine coupling in vicinity.

excitation is also neglected³⁷. $B_{dip}(t) = \frac{\mu_0}{4\pi} \sum_i g_e \mu_B (3cos^2\theta_i - 1)\sigma_i/r_i^3$ is the total magnetic field generated by the target spin(s) at the NV. g_e is the g-value of the target spin. θ_i and r_i are the angle and distance between the NV spin and target spin. B_{dip} is assumed to be constant throughout one evolution period. When the MW2 pulse are not on resonance, it does not drive any state evolution. As the result, the odd and even terms in Eqn. 2 are canceled. On the other hand, when the frequency of MW2 is on resonance, the MW2 pulse flips the target spins. This spin flip changes the sign of B_{dip} in even terms of Eqn.2, i.e. $B_{dip} \rightarrow -B_{dip}$, allowing the phase to accumulate over the total sensing period. Namely, Eqn.2 can be rewritten as,

On Resonance:
$$\delta \phi = \frac{g_{NV} \mu_B}{\hbar} \left[\int_0^{\tau} B_{dip} dt + \int_{\tau}^{3\tau} B_{dip} dt + \dots \right]$$

$$= \frac{g_{NV} \mu_B}{\hbar} \int_0^{16\tau} B_{dip} dt, \qquad (3)$$

Off Resonance: $\delta \phi = 0$.

It is worth to note that even though the bath spins are not polarized to be in the same state in each measurement, we can still observe the NV-EPR signal since it is due to statistical average of the spin polarization instead of a thermal polarization. In general, the NV-EPR signal due a phase shift of $\delta \phi$ is given by,

$$I_{\text{NVEPR}} = \frac{1}{2} \left(1 + \langle \cos(\delta \phi) \rangle \right), \tag{4}$$

where $\langle ... \rangle$ represents the statistical average. In the present case, we consider a case where the phase shifts are caused by the flips of target spins with the application of the MW2 pulses (T_{MW2}). Then, the NV-EPR signal is given by³⁷,

$$I_{\text{NVEPR}} = \frac{1}{2} + \frac{1}{2} exp(-\left(\frac{t}{T_0}\right)^2) \left\langle cos\left(\frac{\mu_0}{4\pi} \frac{\mu_B^2 g_{NV} g_e T_{MW2}}{\hbar} \sum_j \frac{(3cos^2 \theta_j - 1)\sigma_j}{r_j^3}\right) \right\rangle_{\sigma_j}$$

$$= \frac{1}{2} + \frac{1}{2} exp(-\left(\frac{t}{T_0}\right)^2) \left\langle cos\left(\sum_j \omega_j T_{MW2}\right) \right\rangle_{\sigma_j},$$
(5)

where σ_j is +1 or -1 representing $|\uparrow\rangle$ or $|\downarrow\rangle$, respectively. $\langle ... \rangle_{\sigma_j}$ here denotes statistical average of all conditions with different combination of σ_j values. μ_0 is the vacuum magnetic permeability. T_{MW2} is the MW2 pulse duration. ω_j is the Rabi frequency associated with dipole interaction strength. Similar to the experiment in Fig. 2(d), the Gaussian decay is included to take into account a decay in Rabi oscillations 14 where T_0 is the decay constant. When the NV-EPR signal is from a single spin, the oscillations are given by a single sinusoidal function. When it is from two spins, the oscillations are given by a sum of two sinusoidal functions, etc. Therefore, the analysis of the oscillations can be used to determined the number of spins coupled to the NV center as well as their coupling strength.

Next, we introduce another NV-EPR experiment to determine the number of spins and strength of interactions detected in the NV-EPR signal. The sequence is shown in Fig. 5(a). This sequence is modified from the CPMG-DEER sequence to measure the Rabi oscillations of the NV-EPR

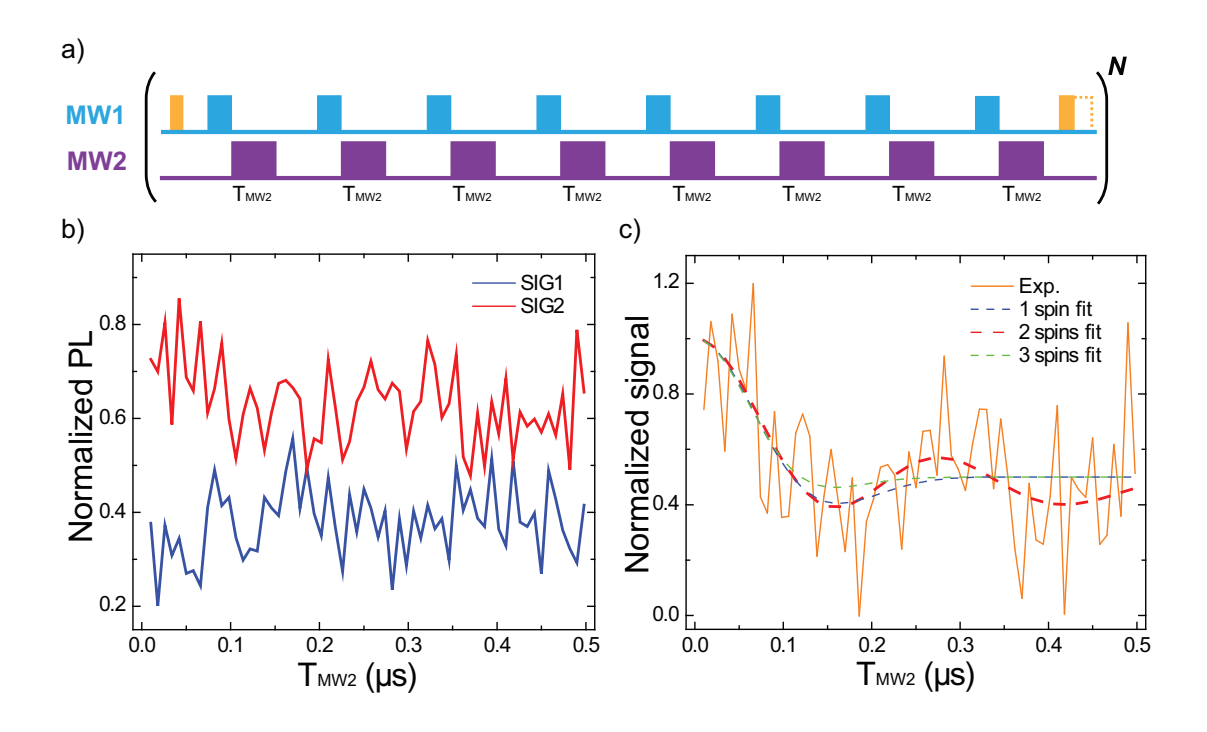


FIG. 5. Rabi oscillation of NV-EPR signal. (a) DEER-Rabi sequence. The length of MW2 pulses are swept. N = 1,260,000. (b) Rabi oscillation of the NV-EPR signal. Both SIG1 and SIG2 PL intensities are normalized same way as previous experiments. (c) The difference (SIG2-SIG1) is normalized from 0 to 1 and then fit to a simple NV-EPR model, where the two electron spins configuration gives the best fit.

signal, so we call it a DEER-Rabi sequence. In the DEER-Rabi sequence, the MW2 frequency is fixed at the EPR signal and the pulse length (T_{MW2}) is varied while keeping the total echo evolution time fixed. Both SIG1 and SIG2 channels are used as well for better SNR. Data is shown in Fig. 5(b). The normalized DEER-Rabi signal (SIG2-SIG1) shows a strong oscillation in the population recovery (shown in Fig. 5(c)). The observed oscillations are due to the change of dipole field from spins felt by NV coherence state. The MW2 pulses rotate the spins according to the pulse length, changing the strength of field along NV axis. The accumulated phase shifts therefore undergo oscillations. To analyze the signal (shown in Fig. 5(c)) with Eqn. 5, we consider three situations where the number of target spins ranges from 1 to 3. In the fit, the dipole interaction strength and decay constant are treated as fitting parameters. The fitted lines are plotted as dotted lines in Fig. 5(c). The adjusted R-square value $(1 - (1 - \frac{\sum (y_i - \hat{y}_i)^2}{\sum (y_i - \hat{y})^2} \frac{n-1}{n-k-1}))$ is used, where k = 3. In general the value is between 0 and 1, and the closer case to 1 means better agreement. The two electron spin model has the best fit with the adjusted R-square value of 0.314 while one spin model gives 0.269 and three spin model gives 0.233. From the fitting result, two interaction strengths are

 $\omega_1=2\pi\times(1.12\pm0.13)$ MHz and $\omega_2=2\pi\times(2.24\pm0.17)$ MHz. The time constant T_0 is fit to be $0.34\pm0.06~\mu s$.

Finally we discuss the origin of the NV-EPR signal observed in the present investigation (see Fig. 4(c) and (d)). The signal is a single peak of coherence population difference centered at 914.7 ± 0.9 MHz with a width of 9 ± 2 MHz. No signature of the hyperfine splitting is observed. We attribute this signal to an electron spin with S = 1/2 and $g = 2.009 \pm 0.003$. Since there are no signature of hyperfine peaks, the signal is not from P1 centers, which are commonly observed in diamond with a high nitrogen concentration. The identification of the detected spins remains unclear, but based on the S and g-value and lack of the hyperfine splitting, possible candidates of the observed spins are the tri-Nitrogen W21 center^{38,39} and surface spins^{32,40,41}.

IV. SUMMARY

In summary, we demonstrated the detection of EPR from two electron spins using a single NV center in diamond. CPMG-DEER and DEER-Rabi sequences are used to study the spin interactions. The observed NV-EPR signal is in absence of strong hyperfine peaks, and further measurement of Rabi oscillations of the signal suggests the interaction is of a single NV center with two electron spins. The physical system and method presented in this paper allows easy identification of single defect center coupled to a small number of spins and characterization of the interaction strength. The analysis of NV-EPR signal presented can be a method to distinguish the number of interacting spins up to five, which is limited by the detection time window of the oscillations.

The non-equal but measurable interaction strength is favorable in studying non-equilibrium quantum dynamics. Investigation of quantum phase dynamics, like spin liquids or discrete time crystalline (DTC), requires interacting spin system with disordered structures^{24,27}. Cu²⁺ ions formed kagome lattice⁴² and Ru³⁺ ions formed honeycomb lattice⁴³ has been actively researched materials for realization of spin liquid. This multi electron spin system could be a material to look for these emergent quantum effects with the similarity of being a spin 1/2 magnetic disordered type of material. A chain of 9 ¹³C nuclear spins in diamond has been shown to be a programmable spin-based DTC⁴⁴. The characterizable electron spin system in this study is potentially a smaller sized system to realize DTC. A good knowledge of the interaction strengths in a spin system will also be significant in better characterization of non-classical correlations, namely quantum entanglement, which can be key in modeling open quantum dynamics and developing entangled quantum sens-

ing. Quantum enhanced NMR with a 9.4-fold of sensitivity increase has been demonstrated by entangling 9 proton spins with a ³¹P spin⁴⁵. The electron spins detected in this study can also be simultaneously controlled and potentially achieve entanglement enhancement beyond the standard quantum limit. In addition, further study can be done to reveal more information about the nature of the spin species and improve the understanding of decoherence of shallow NV centers, paving the pathway to higher standard engineering for quantum sensing applications.

ACKNOWLEDGMENTS

This work was supported by the National Science Foundation (ECCS-2204667 and CHE-2004252 with partial co-funding from the Quantum Information Science program in the Division of Physics), the USC Anton B. Burg Foundation, and the Searle scholars program (ST).

DATA AVAILABILITY

The data that support the findings of this study are available from the corresponding author upon reasonable request.

REFERENCES

- ¹A. Gruber, A. Dräbenstedt, C. Tietz, L. Fleury, J. Wrachtrup, and C. von Borczyskowski, Science **276**, 2012 (1997).
- ²F. Jelezko, T. Gaebel, I. Popa, A. Gruber, and J. Wrachtrup, Phys. Rev. Lett. **92**, 076401 (2004).
- ³T. Gaebel, M. Domhan, I. Popa, C. Wittmann, P. Neumann, F. Jelezko, J. R. Rabeau, N. Stavrias, A. D. Greentree, S. Prawer, J. Meijer, J. Twamley, P. R. Hemmer, and J. Wrachtrup, Nat. Phys. **2**, 408 (2006).
- ⁴L. Childress, M. V. G. Dutt, J. M. Taylor, A. S. Zibrov, F. Jelezko, J. Wrachtrup, P. R. Hemmer, and M. D. Lukin, Science **314**, 281 (2006).
- ⁵S. Takahashi, R. Hanson, J. van Tol, M. S. Sherwin, and D. D. Awschalom, Phys. Rev. Lett. **101**, 047601 (2008).
- ⁶G. Balasubramanian, P. Neumann, D. Twitchen, M. Markham, R. Kolesov, N. Mizuochi, J. Isoya, J. Achard, J. Beck, J. Tissler, V. Jacques, P. R. Hemmer, F. Jelezko, and J. Wrachtrup, Nat. Mater. **8**, 383 387 (2009).

- ⁷G. de Lange, Z. H. Wang, D. Ristè, V. V. Dobrovitski, and R. Hanson, Science **330**, 60 (2010).
- ⁸C. L. Degen, Appl. Phys. Lett. **92**, 243111 (2008).
- ⁹G. Balasubramanian, I. Y. Chan, R. Kolesov, M. Al-Hmoud, J. Tisler, C. Shin, C. Kim, A. Wojcik, P. R. Hemmer, A. Krueger, T. Hanke, A. Leitenstorfer, R. Bratschitsch, F. Jelezko, and J. Wrachtrup, Nature **455**, 648 (2008).
- ¹⁰J. R. Maze, P. L. Stanwix, J. S. Hodges, S. Hong, J. M. Taylor, P. Cappellaro, L. Jiang, M. V. G. Dutt, E. Togan, A. S. Zibrov, A. Yacoby, R. L. Walsworth, and M. D. Lukin, Nature 455, 644 (2008).
- ¹¹J. M. Taylor, P. Cappellaro, L. Childress, L. Jiang, D. Budker, P. R. Hemmer, A. Yacoby, R. Walsworth, and M. D. Lukin, Nat. Phys. 4, 810 (2008).
- ¹²M. S. Grinolds, S. Hong, P. Maletinsky, L. Luan, M. D. Lukin, R. L. Walsworth, and A. Yacoby, Nat. Phys. **9**, 215 (2013).
- ¹³F. Shi, Q. Zhang, P. Wang, H. Sun, J. Wang, X. Rong, M. Chen, C. Ju, F. Reinhard, H. Chen, J. Wrachtrup, J. Wang, and J. Du, Science 347, 1135 (2015).
- ¹⁴C. Abeywardana, V. Stepanov, F. H. Cho, and S. Takahashi,
 J. Appl. Phys. **120** (2016), 10.1063/1.4963717.
- ¹⁵B. Fortman, L. Mugica-Sanchez, N. Tischler, C. Selco, Y. Hang, K. Holczer, and S. Takahashi, J. Appl. Phys. **130**, 083901 (2021).
- ¹⁶B. Fortman and S. Takahashi, J. Phys. Chem. A **123**, 6350 (2019).
- ¹⁷B. Fortman, J. Pena, K. Holczer, and S. Takahashi, Appl. Phys. Lett. **116**, 174004 (2020).
- ¹⁸S. Li, H. Zheng, Z. Peng, M. Kamiya, T. Niki, V. Stepanov, A. Jarmola, Y. Shimizu, S. Takahashi, A. Wickenbrock, and D. Budker, Phys. Rev. B **104**, 094307 (2021).
- ¹⁹Y. Ren, C. Selco, D. Kawashiri, M. Coumans, B. Fortman, L.-S. Bouchard, K. Holczer, and S. Takahashi, Phys. Rev. B **108**, 045421 (2023).
- ²⁰J. Cai, A. Retzker, F. Jelezko, and M. B. Plenio, Nat. Phys. **9**, 168 (2013).
- ²¹Y. Wang, F. Dolde, J. Biamonte, R. Babbush, V. Bergholm, S. Yang, I. Jakobi, P. Neumann, A. Aspuru-Guzik, J. D. Whitfield, and J. Wrachtrup, ACS Nano 9, 7769 (2015).
- ²²C. Ju, C. Lei, X. Xu, D. Culcer, Z. Zhang, and J. Du, Phys. Rev. B **89**, 045432 (2014).
- ²³T. Xie, Z. Zhao, X. Kong, W. Ma, M. Wang, X. Ye, P. Yu, Z. Yang, S. Xu, P. Wang, Y. Wang, F. Shi, and J. Du, Sci. Adv. 7, eabg9204 (2021).
- ²⁴C. Broholm, R. J. Cava, S. A. Kivelson, D. G. Nocera, M. R. Norman, and T. Senthil, Science **367**, eaay0668 (2020).

- ²⁵S. Choi, J. Choi, R. Landig, G. Kucsko, H. Zhou, J. Isoya, F. Jelezko, S. Onoda, H. Sumiya, V. Khemani, C. von Keyserlingk, N. Y. Yao, E. Demler, and M. D. Lukin, Nature 543, 221+ (2017).
- ²⁶F. J. González, A. Norambuena, and R. Coto, Phys. Rev. B **106**, 014313 (2022).
- ²⁷S. Bussandri, D. Shimon, A. Equbal, Y. Ren, S. Takahashi, C. Ramanathan, and S. Han, J. Am. Chem. Soc. **146**, 5088 (2024).
- ²⁸T. Yamamoto, C. Müller, L. P. McGuinness, T. Teraji, B. Naydenov, S. Onoda, T. Ohshima, J. Wrachtrup, F. Jelezko, and J. Isoya, Phys. Rev. B 88, 201201 (2013).
- ²⁹F. Shi, Q. Zhang, B. Naydenov, F. Jelezko, J. Du, F. Reinhard, and J. Wrachtrup, Phys. Rev. B **87**, 195414 (2013).
- ³⁰A. Cooper, W. K. C. Sun, J.-C. Jaskula, and P. Cappellaro, Phys. Rev. Lett. **124**, 083602 (2020).
- ³¹E. L. Rosenfeld, L. M. Pham, M. D. Lukin, and R. L. Walsworth, Phys. Rev. Lett. **120**, 243604 (2018).
- ³²M. S. Grinolds, M. Warner, K. De Greve, Y. Dovzhenko, L. Thiel, R. L. Walsworth, S. Hong, P. Maletinsky, and A. Yacoby, Nat. Nanotechnol. 9, 279 (2014).
- ³³A. O. Sushkov, I. Lovchinsky, N. Chisholm, R. L. Walsworth, H. Park, and M. D. Lukin, Phys. Rev. Lett. **113**, 197601 (2014).
- ³⁴X. Xiao and N. Zhao, New J. Phys. **18** (2016), 10.1088/1367-2630/18/10/103022.
- ³⁵Y. Dakir, A. Slaoui, A.-B. A. Mohamed, R. A. Laamara, and H. Eleuch, Sci. Rep. **13**, 20526 (2023).
- ³⁶Qnami, "Quantum sensing leaders in nanoscale precisionlynami," https://qnami.ch/(2024).
- ³⁷V. Stepanov and S. Takahashi, Phys. Rev. B **94**, 024421 (2016).
- ³⁸J. H. N. Loubser and J. A. van Wyk, Rep. Prog. Phys. **41**, 1201 (1978).
- ³⁹J. M. Baker, Radiat. Eff. Defects Solids **150**, 415 (1999).
- ⁴⁰Z. Peng, T. Biktagirov, F. H. Cho, U. Gerstmann, and S. Takahashi, J. Chem. Phys. **150**, 134702 (2019).
- ⁴¹Z. Peng, J. Dallas, and S. Takahashi, J. Appl. Phys. **128**, 054301 (2020).
- ⁴²M. R. Norman, Rev. Mod. Phys. **88**, 041002 (2016).
- ⁴³H. Takagi, T. Takayama, G. Jackeli, G. Khaliullin, and S. E. Nagler, Nat. Rev. Phys. **1**, 264 (2019).
- ⁴⁴J. Randall, C. E. Bradley, F. V. van der Gronden, A. Galicia, M. H. Abobeih, M. Markham, D. J. Twitchen, F. Machado, N. Y. Yao, and T. H. Taminiau, Science 374, 1474 (2021).

⁴⁵J. A. Jones, S. D. Karlen, J. Fitzsimons, A. Ardavan, S. C. Benjamin, G. A. D. Briggs, and J. J. L. Morton, Science **324**, 1166 (2009).